Nanoscale Advances

ROYAL SOCIETY OF CHEMISTRY

PAPER

View Article Online
View Journal | View Issue

Cite this: *Nanoscale Adv.*, 2021, **3**, 2529

All-lignin converted graphene quantum dot/graphene nanosheet hetero-junction for high-rate and boosted specific capacitance supercapacitors†

Zheyuan Ding, Xiuwen Mei and Xiluan Wang *

The high value-added conversion of biomass lignin has been paramount in the field of lignin utilization, especially for high performance energy conversion and storage devices. A majority of lignin-based supercapacitors generally exhibit inferior electrochemical performance with low capacitance and slow diffusion kinetics due to the poor interfacial compatibility, low conductivity, and uncontrollable morphology. Herein, we designed all-lignin converted graphene quantum dot and graphene sheet (GQD/Gr) hetero-junction for simultaneous fast charging and boosted specific capacitance. The conversion from lignin to GQDs and then refusion into graphene allows the *in situ* growth of GQDs on graphene, endowing good interfacial compatibility with the GQD/Gr hetero-junction. Furthermore, both GQDs and graphene sheets exhibit highly crystalline structure with obvious graphene lattice, giving GQDs/Gr good conductivity. GQDs play an additive role for avoiding stacks and agglomerates between graphene layers, which endow the assembled GQDs/Gr with massive electron capacitive sites and more hierarchical channels. Therefore, the GQD/Gr hetero-junction gives rise to a high specific capacitance of 404.6 F g^{-1} and a short charging time constant (τ_0) of 0.3 s, 2.5 times higher and 7.5 times faster than that of the unmodified lignin electrode with 162 F g^{-1} and 2.3 s, respectively. This proposed strategy could offer the opportunity to unblock the critical roadblocks for a superior electrochemical performance lignin-based supercapacitor by composing a 0D/2D GQD/Gr hetero-junction system and also paves a bright way for the high-value industrial lignin conversion into cheap, scalable, and high-performance electrochemical energy devices.

Received 6th December 2020
Accepted 5th March 2021

DOI: 10.1039/d0na01024c

rsc.li/nanoscale-advances

1 Introduction

Supercapacitors are considered as promising energy storage systems for next-generation intelligent vehicles and portable electronics with high power density and long lifespan.[1–3] The development of green, low-cost, and renewable supercapacitors for miniaturized electrics and portable devices have raised increasing interests for fast and efficient electrochemical conversion and storage.[2–4] The use of sustainable, economical, and high-performance natural biomass materials has become a growing demand for next-generation supercapacitors.

Lignin is frequently considered as a biomass byproduct from black liquor that is abandoned or burnt in the pulping and paper industry; however, it deserves more exploration than its current valorization. Lignin extracted from black liquor is generally consists of three units, namely the coniferyl (G) unit, sinapyl alcohol (S) unit, and *p*-hydroxybenzoate (H) unit[5–7] mutually linked by C–O–C and C–C bond linkages, which are vulnerable to alkali pulping.[7,8] It is worth mentioning that alkali lignin from grass pulping black liquor could be easily stimulated by alkali hydrothermal treatment because of the fragile *p*-hydroxy-cinnamic acid (*p*CA) unit-based ester linkages, thus easily producing condensed aromatics.[9] There are several reports about lignin-derived aromatic materials that present highly crystalline and conductive characteristics.[9,10] Its intrinsic aromatic components and condensed aromatics endow it with great potential to convert into conductive materials for further high-valued energy device applications.[9–13] Due to the high molecular weight and amorphous structure, lignin-derived electrodes typically showed low specific surface area, uneven pore distribution, and uncontrollable morphology, which directly led to low capacitance and inferior electrochemical performance.[14–16] Some advances showed promise for superior electrode material preparation.[17–24] Recent publications report the hybrid structure of lignin combined with conductive carbon materials, such as carbon nanotubes and graphene, which present slight contribution towards the electrochemical performance because of the poor interaction between lignin and these materials.[25,26] The strong and stable interaction between lignin and carbon materials was proven to be much more difficult in spite of the rational designs.[26,27] These

Beijing Key Laboratory of Lignocellulosic Chemistry, Beijing Forestry University, Beijing, 100083, P. R. China. E-mail: wangxiluan@bjfu.edu.cn

† Electronic supplementary information (ESI) available: Fig. S1–S5, Tables S1, S2 and ESI References. See DOI: 10.1039/d0na01024c

limitations drive researchers to try and directly transform lignin into a multidimensional structure (0D, 1D, and 2D), such as nanosheets, nanotubes, or nanospheres,[1,16,28–33] aiming at improving the conductivity and drawing support from the frame structure. It is highly suggested that the sheet-like morphology could enable highly efficient ionic diffusion and increased numbers of active sites for the sheet-like morphology could enable highly efficient ionic diffusion and increased numbers of active sites for ion storage.[3] However, the inevitable π–π stacks could easily deteriorate ion storage and diffusion, thus delivering negative effects on the electrochemical property.[29,34–38] The lignin-based graphene sheet used for supercapacitors inevitably produced numerous stacks and irreversible agglomerates for the sheets similar to graphene-based electrode behavior.[27,34–37] These concerns stand a block for the development of high performance all-lignin based supercapacitors, which have been rarely solved or reported before. Therefore, the rational construction of lignin-based nanosheets avoiding aggregates could be the moderate strategy including hetero-junction intercalation or hetero-atom doping.[27,39,40]

Herein, we propose a facile, low-cost, and scalable method to construct a hetero-junction of GQDs and graphene (GQDs/Gr) totally derived from lignin (Scheme 1) to boost the high specific capacitance and ultrafast charging speed. The conversion from lignin to GQDs and then GQDs' refusion into the graphene sheet gives the *in situ* growth of GQDs on the graphene sheet, endowing a good interfacial compatibility between the GQDs and Gr. The GQDs nano-additive strategy against the stacks and agglomerates was advocated to acquire highly dispersed graphene sheets, allowing for more electron storage and efficient diffusion for the assembled GQD/Gr electrode. Both the GQDs and graphene sheet present a highly crystalline character, which is greatly helpful for constructing highly conductive electrode. The GQD/Gr hetero-junction with good interfacial compatibility, controlled morphology, and high conductivity exhibit simultaneously boosted specific capacitance and fast charging speed with a high specific capacitance of 404.6 F g^{-1} and short charging time constant (τ_0) of 0.3 s among all the lignin-based supercapacitor, which is also 2.5 times higher and 7.5 times faster than that of unmodified lignin electrode with 162 F g^{-1} and 2.3 s, respectively. The proposed 0D/2D GQD/Gr hetero-junction solve the critical limits for all lignin-based high-performance supercapacitor, and pave a bright way for high valued utilization of industrial lignin into cheap, sustainable, and high-performance electrochemical energy devices.

2 Experimental

2.1 Materials and methods

The alkali lignin (AL) was extracted from pulping black liquor of grass (*Hybrid Pennisetum*) and the AL was obtained through acid precipitation, which is the same as that in our previous reports.[9] In brief, black liquor (alkali pulping) was firstly neutralized at a pH of approximately 5 with 10% H_2SO_4 and then 10 times volume of acid was added dropwise under persistent stirring, maintaining a pH of 1–2. The lignin precipitate was subsequently washed 5 times with acid and deionized water. Lignin was finally obtained after freeze-drying.

2.2 Preparation of GQDs/Gr

The GQD/Gr synthetic method was developed based on our previous *in situ* activation method.[9,10] In brief, the resultant 5 g AL was dissolved in 2 M NaOH, and then 50 mL of AL solution was ultrasonicated for 30 min, which was finally transferred into a Teflon-lined autoclave and heated at 180 °C for 9 h. After cooling to room temperature, the obtained solution was filtered and washed with deionized water. The GQD/Gr suspension in water was obtained after centrifugation (5000 rpm, 30 min) to remove the insoluble carbons. Finally, it was purified by dialysis (retained molecular weight: 3000 Da) for 3 days. GQDs/Gr was finally obtained after freeze-drying.

2.3 Activation of GQDs/Gr

The freeze-dried GQD/Gr powder was mixed with KOH in the ratio of 1 : 2 and the mixture was activated in the tube furnace using the following procedure: room temperature to 500 °C at a heating rate of 10 °C min^{-1} and maintained for 1 h, then from

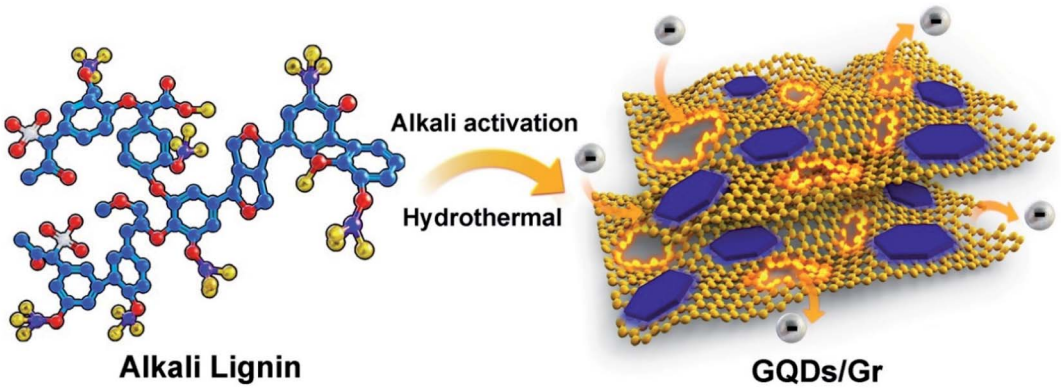

Scheme 1 An all-lignin converted 0D/2D GQD/Gr hetero-junction was designed by facile, low cost, and scalable alkali activation hydrothermal method for high rate and boosted specific capacitance supercapacitor.

500 to 800 °C at a heating rate of 5 °C min^{-1}, and maintained at 800 °C for 2 h, and finally cooled down to room temperature at a heating rate of 10 °C min^{-1}.

2.4 Characterization

Transmission electron microscopy (TEM) was performed on a Hitachi H-7650B TEM operating at 80 kV. The high-resolution transmission electron microscope (HR-TEM) image was taken using a FEI Tecnai F20 HR-TEM operating at 200 kV. The AFM image was acquired by a Bruker MultiMode 8 AFM equipment. The X-ray diffraction (XRD) patterns were obtained with a Bruker D8 using Cu Kα radiation (60 kV, 80 mA, $\lambda = 1.5418$ Å). The Fourier transform infrared (FT-IR) spectra were recorded by a Nicolet iN10 FT-IR spectrometer with a resolution of 4 cm^{-1}. The Raman spectra were measured on a LabRAM HR Evolution Raman spectrometer using a 532 nm laser beam. The X-ray photoelectron spectra (XPS) experiments were undertaken on an ESCALAB 250Xi photoelectron spectrometer using Al Kα (1486.6 eV) radiation. The electrochemical property was studied on a ChenHua CHI760e electrochemical workstation and a CT2001A LAND battery test system. ^{1}H and ^{13}C heteronuclear single quantum coherence (HSQC) NMR spectra were acquired on a Bruker AVIII 400 MHz spectrometer. The preparation of the NMR testing samples was similar with our previous sampling methods.[9,41] In brief, the dried GQD/Gr sample (40 mg) was dissolved in D_2O (0.5 mL) with ultrasonication for 10 min and the homogeneous solution was transferred into a 5 mm NMR tube for subsequent analysis under the Bruker pulse program.

2.5 Electrochemical measurement

The homogeneous slurry was composed of activated GQD/Gr powder, carbon black, and 5% polytetrafluoroethylene (PTFE) solution in the ratio of 8 : 1 : 1. The slurry was uniformly coated on nickel foam with 10 MPa pressure and then dried at 60 °C for 12 h to obtain the working electrode. Two similar pieces of electrodes with an area of 1.0 cm^2 were chosen as the working electrode. The two-electrode system was performed on the cell composed of an electrode, active components (single electrode containing about 3 mg), electrolyte (2 M Li_2SO_4), and separator (cellulose paper). The three-electrode system was assembled in a three-electrode cell with a counter electrode (platinum foil), a reference electrode (Hg/HgO electrode), and the electrolyte (6 M KOH solution).

The CV curves were obtained under scan rates from 5 to 200 mV s^{-1} in the voltage window of −1 to 0 V and 0–1 V for three and two electrode systems. The galvanostatic (GCD) charge/discharge test was performed under different current densities in the range of 0.1–50 A g^{-1}. Similarly, the CV and GCD curves were obtained on the cell with the same working conditions as that of the three-electrode system.

The specific capacitance was calculated according to the formula

$$C_{m_3}\ (\mathrm{F\ g^{-1}}) = \frac{I \times \Delta t}{\Delta V \times m} \quad \text{and} \quad C_{m_2}\ (\mathrm{F\ g^{-1}}) = \frac{2 \times I \times \Delta t}{\Delta V \times m}$$

where C_{m_3} and C_{m_2} are the specific capacitance for three and two electrode systems, and I (A), ΔV (V), Δt (s), and m (g) stand for discharge current, voltage range, discharge time, and mass of one single electrode, respectively.

The EIS measurements were carried out in the frequency range from 10 mHz to 100 kHz at the open circuit potential of 5 mV amplitude. The cycle stability test was performed at current densities of 10 A g^{-1} for 10 000 charge/discharge cycles on the assembled cell by the LAND battery test system. The relationship between the time constant (τ_0) and the characteristic frequency (f_0) was equal to $\tau_0 = 1/f_0$.

3 Results and discussion

The electrochemical performance could be directly decided by the crystallinity and morphology of the electrode materials, which are highly related to the conductivity and porosity, respectively.[25,26] Typically, the synthesis of the biomass-based graphene sheet is easily performed by hydrothermal reforming from biomass waste lignin *via* an *in situ* alkaline activation-synthesis method, which is developed and modified according to our previous reports.[9,10] By carefully modifying the hydrothermal period and the alkali concentration, the GQD/Gr sheet could be toiled with both high crystallinity and porosity. The typically layered morphology for the GQD/Gr sheet with a single layered thickness of ~1 nm could be observed with ~5 μm

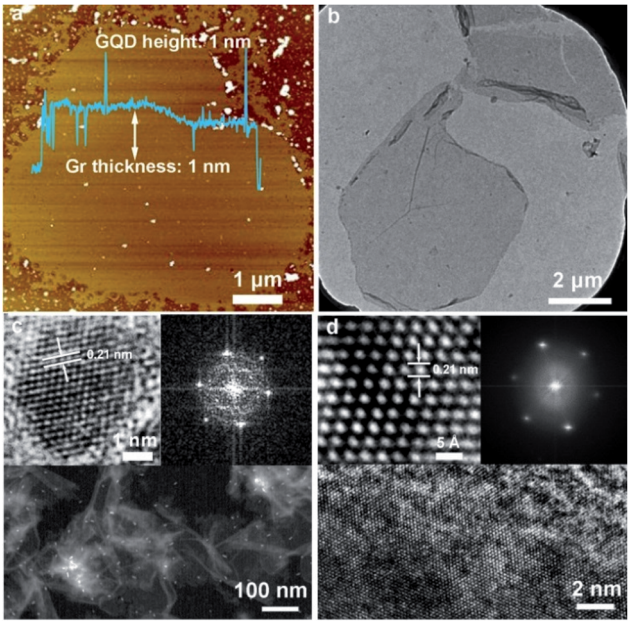

Fig. 1 (a) The AFM image of graphene sheets and GQDs derived from black liquor, showing the consistent refusion from the GQDs to the porous graphene sheet and then converted into GQDs/Gr. (b) TEM images of GQDs/Gr. (c) Top: the enlarged high-resolved HR-TEM image towards the GQDs lattice (left) and the FFT pattern (right). Bottom: the HAADF-STEM image of GQDs/Gr. (d) Top: the atomic resolved HR-TEM image of the graphene lattice (left) and the FFT pattern (right) to show the well-ordered honeycomb lattice structure with a lattice spacing of 0.21 nm. Bottom: the magnified HR-TEM images indicated a large area well-ordered graphene lattice.

lateral size from the AFM image (Fig. 1a). In spite of the micron-sized nanosheets, the existence of extremely small graphene quantum dots (GQDs) or graphene islands of ~1 nm height and obvious pore defects could also be noticed around the GQD/Gr plane. High-resolution AFM images and profiles were provided towards different GQDs/Gr within multiple directions (Fig. S1 and S2†), which is indicative of the existence of many pores and GQDs located on the GQD/Gr plate. It is implied that numerous GQDs may be gradually co-fused and self-assembled around the GQD/Gr edge, directly inducing intrinsic pore defects during the hydrothermal co-fusing period, as shown in the AFM. These nano porous channel could facilitate the development of a connected porous structure for the preparation of the electrode.[9,27,42] A representative TEM image in Fig. 1b also depicts its lamellar character with obvious folds located in the plane of the sheet. The uniform dispersion of the GQDs with several to dozen nanometers around the GQDs/Gr also could be noticed. Similarly, the smaller GQD/Gr sheets around the GQDs/Gr also reflect the existence of uniformly dispersed GQDs, which conformed well with the AFM characterization.

Furthermore, the fine structure of crystalline and hetero-GQD/Gr hybrid was verified by HRTEM. The HAADF-STEM mode image reflected the GQD/Gr hybrid in Fig. 1c and the GQDs were uniformly dispersed around the GQD/Gr sheet. The well-ordered graphene lattice and the hexagonal FFT pattern (inset of Fig. 1c) toward single GQD observed in the enlarged HRTEM image reflect the typical crystalline feature of graphene.[9,10,43–45] Moreover, we further characterized the single GQD/Gr sheet and the HR-TEM image located in the plane of GQDs/Gr could give a clear observation of the large area well-ordered graphene lattice hybrid with some obvious pore defects (Fig. 1d). The HRTEM and FFT pattern (inset of Fig. 1d) exhibited the atomically resolved 6-ring graphitic network with the 0.21 nm lattice parameter, directly proving the crystalline lattice similar to graphene[9,10,43,44] in spite of the weak FFT signal within one direction, which is mainly caused by the defects. Overall, the AFM and HRTEM images give a clear description of the GQD/Gr hetero-junction, in which the GQD/Gr sheet exhibits a large area well-ordered graphene lattice with some pore defects and the typical GQDs' crystalline feature. The crystalline GQD/Gr hetero-junction endow electrode with the good porosity and high conductivity, owning great potential for increased numbers of active sites for ion storage and efficient charge diffusion in supercapacitors, respectively.

It is well recognized that lignin can easily generate aromatic condensation during the long-period hydrothermal treatment.[9,10,46–49] The 2D-HSQC NMR spectra were introduced to explain the mechanism towards the formation of GQDs/Gr from the molecular viewpoint. The typical $S_{2,6}$, G_2, G_5, G_6, and $H_{2,6}$ signals in AL at 104/6.66 ppm, 111.4/6.96 ppm, 115.5/6.69 ppm, 119/6.8 ppm, and 128.5/7.03 ppm, respectively, were greatly weakened, and the *p*CA signal including the pCA_α, pCA_β/$pCA_{3,5}$, and $pCA_{2,6}$ signals located at 117/6.4, 130/7.53, and 144.2/7.5 ppm, respectively, totally disappeared, which were considered as the active site for aromatic refusion (Fig. 2a–c).[9] The AFM images (Fig. 1a and S1†) evidence the corresponding refusion process with many assembled sheet fragments around the edge, which could also be noticed in the HRTEM (Fig. 1c) image. Furthermore, new peak signals representing sp^2 hybrid aromatic conjugation (Fig. 2d with ★ symbol) at 130.9/6.53 and 135.3/6.48 ppm were generated (Fig. 2b).[9,50,51] We could infer that *in situ* alkaline activation reaction firstly converted the lignin into some GQDs reflected in the peak at 130.9/6.99 ppm corresponding to the aromatic characteristic peak of GQDs,[10] which is located in the Gr plane seen in the AFM profile (Fig. 1a and S1†) and the HRTEM image (Fig. 1c). The resultant GQDs were continuously converted into porous graphene sheet by aromatic enlargement and finally *in situ* assembled into the GQD/Gr hetero-junction reflected at 135.3/6.48 ppm, corresponding to the aromatic region.[9,50,51]

Therefore, the assembled mechanism could be summarized in three steps: (I) lignin aromatic rebonding, (II) aromatic

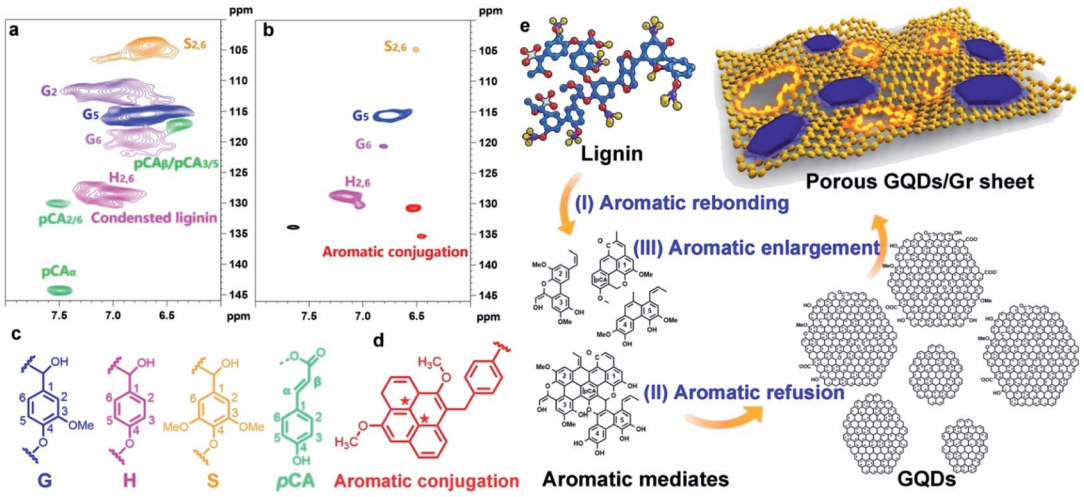

Fig. 2 The 2D-HSQC NMR spectra of (a) AL and (b) GQDs/Gr, (c) Left to right: G, H, S, and *p*CA unit (d) generated aromatic conjugation in the GQD/Gr sheets. (e) Possible mechanism from lignin to GQD/Gr sheet including (I) lignin aromatic rebonding, (II) aromatic refusion into the GQDs, and (III) aromatic enlargement of the GQDs aromatic enlargement into the porous GQD/Gr sheet.

refusion into the GQDs, and (III) GQDs aromatic enlargement into the GQD/Gr hetero-junction (Fig. 2e). The GQDs as the crystal nuclei for larger aromatic conjugation were likewise graphene islands in the CVD-grown method for large size graphene,[52,53] which was further consistent with the AFM characterization illustrated as the co-fusion process (Fig. 1a).

The XPS and FT-IR spectra could reflect the detailed chemical composites of GQDs/Gr. The survey XPS spectrum of GQDs/Gr (Fig. 3a) shows typical C 1s and O 1s signals with a C : O atomic ratio of 2.8. The high resolution C 1s spectrum (Fig. 3b) exhibits three fitted peaks including the predominant C=C peak (284.7 eV), strong C–O peak (286.2 eV), and C=O (288 eV), and the deconvolution of the O 1s peak (Fig. 3c) displays the C=O and C–O peaks located at 531 eV and 532.8 eV, respectively. The FT-IR spectrum (Fig. 3d) also gave a typical band vibration of graphene features with broad O–H stretching vibration (3000–3700 cm^{-1}), C=O vibration (1720 cm^{-1}), C=C vibration (1585 cm^{-1}), and C–O vibration (1218 cm^{-1}), which matched well with the XPS spectra.

The large-area graphitic structure was further characterized by XRD and Raman spectroscopy. An intensive peak at approximately 27° corresponding to the (002) peak (Fig. S3†) well evidences its crystalline feature. Furthermore, the D peak at 1347 cm^{-1} and G peak at 1564 cm^{-1} corresponding to the defects and crystallinity were noticed, as shown in Fig. 3e, respectively. The prominent D peak attributed to the defect effect of the sp^2-hybridized carbon rings' breathing mode and the G peak is associated with the stretching of sp^2-hybridized carbon pairs. The intensity ratio of the D to the G peak of 0.73 reflected into the in-plane structure of the large-area sp^2-hybridized domains decorated with some defects, which well conformed with the AFM and HR-TEM data. It is suggested that this crystalline structure with defects is much favorable for the capacitive performance.[54,55]

The specific surface area and pore distribution was highly relevant to the capacitive performance.[23] The specific surface area in the Brunauer–Emmett–Teller (BET) mode was calculated as 1393 $m^2\ g^{-1}$ from the N_2 adsorption–desorption isotherms following I type isotherm, according to the IUPAC in Fig. 3c. The pore distribution (inset of Fig. 3c) indicated that a majority of pores are smaller than 2 nm, corresponding to the micropores, and only 8% portion of the pores belong to the mesoporous region (2–50 nm). The highly dispersed GQD/Gr sheet with the additives of GQDs provide an abundantly interconnected nano channel, thus enhancing the specific surface area. The enhanced specific surface area and abundant micropores shorten the conductive distance and speed up the charge diffusion, allowing for good electrochemical performance.

These nano porous channels constructed the highly connected porous structure, and the GQDs and the graphene sheet could generate the GQD/Gr hetero-junction, thus facilitating the increase of active sites for ion storage and diffusion. In addition, the GQDs function as an additive between the graphene layers for the effective prevention of stack formation, thus efficiently enlarging the distance between the graphene layers. The retained nanosheet morphology enables highly efficient ionic diffusion and increased numbers of active sites for ion storage.[3] The larger specific surface area of the GQDs/Gr could provide more favorable porous networks for ion diffusion for the improvement of electrical capacitance. The specific capacitance

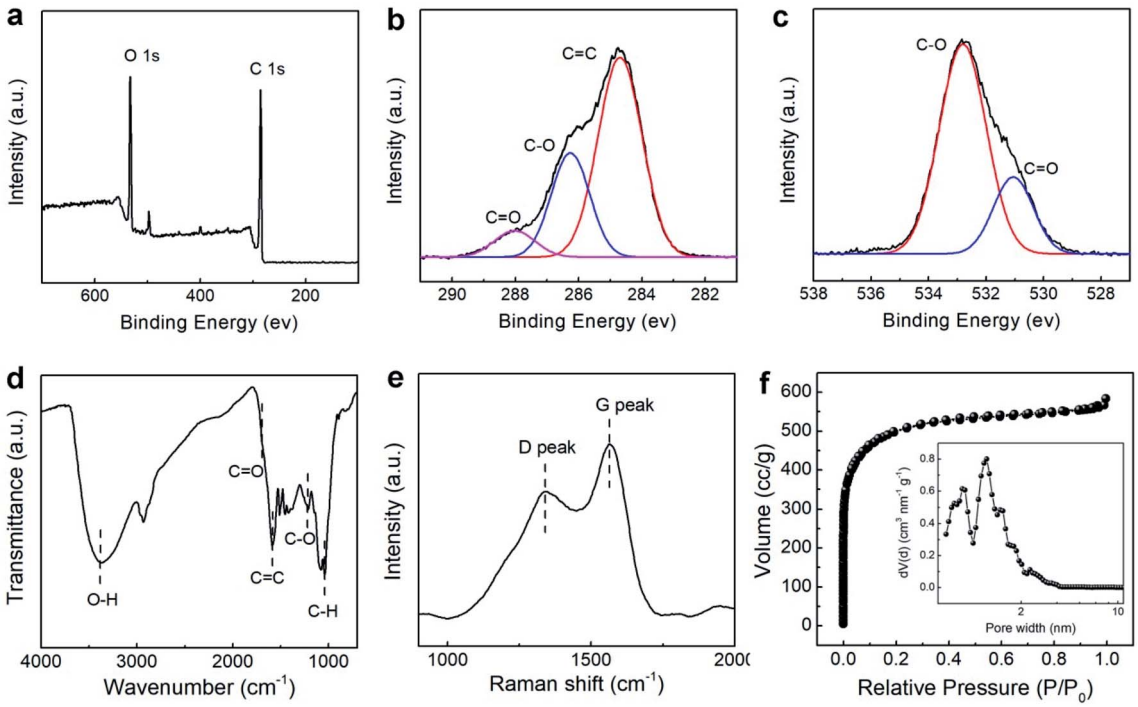

Fig. 3 (a) XPS survey of GQDs/Gr. High resolution XPS spectra of (b) C 1s and (c) O 1s. (d) FT-IR spectrum of GQDs/Gr, (e) Raman spectrum of GQDs/Gr, (f) N_2 adsorption–desorption isotherms, inset: pore distribution of GQDs/Gr.

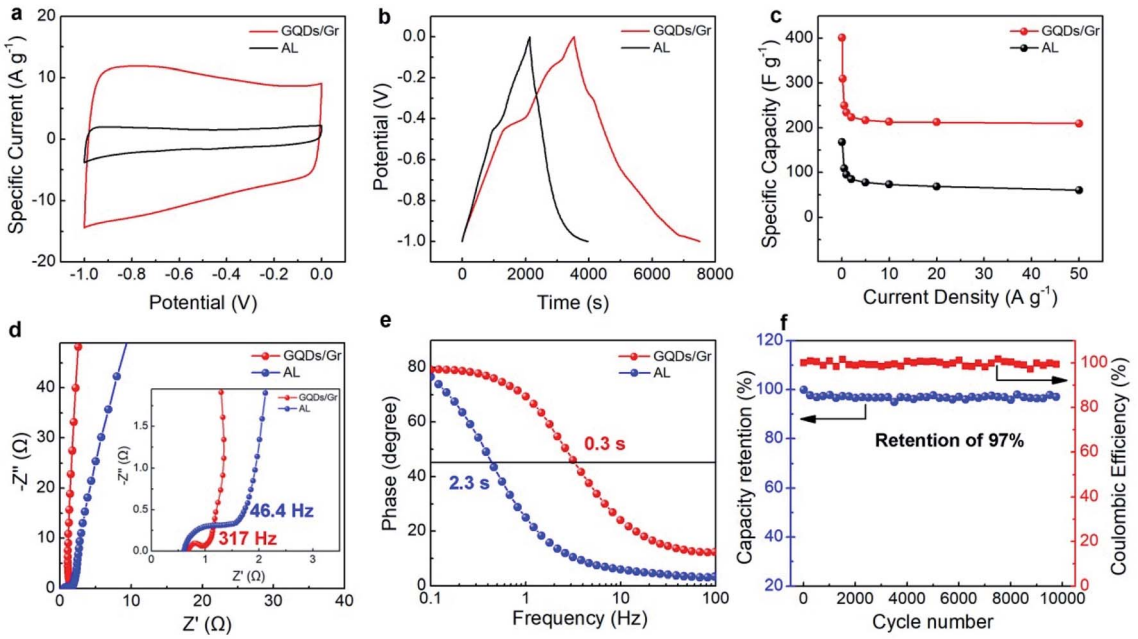

Fig. 4 Electrochemical property of the GQDs/Gr and AL-based supercapacitor, (a) CV curve at a scan rate of 50 mV s^{-1} (b) galvanostatic charge/discharge curves at a current density 0.1 A g^{-1}. (c) Rate capacity under different current density (d) Nyquist plots and (e) Bode plots phase angle *versus* frequency (f) cycle stability at a current density of 10 A g^{-1}.

of GQDs/Gr and AL was evaluated by cyclic voltammetry (CV) tests. As shown in Fig. 4a, both the GQDs/Gr and AL shown in the CV curve indicate an obvious improvement for the specific capacitance.

The specific capacitances were further calculated by the galvanostatic charge/discharge cycling (GCD) curve. Fig. 4b shows a non-rectangular shape corresponding to the behavior of pseudocapacity apart from the EDLC capacitance. An obvious charging platform at −0.5 V could be attributed to the pseudocapacity from oxygenate groups. As shown in Fig. 4c, the specific capacitance exhibits an obvious improvement. The GQD/Gr-based supercapacitor shows a high specific capacitance of 404.6 F g^{-1} (0.1 A g^{-1}) among all lignin-converted supercapacitors (Tables S1 and S2†), which is 2.5 times greater than that of the AL-based supercapacitor (162 F g^{-1}). This could be attributed to the improved specific surface area with abundant connected nano channels, thus enhancing the capability of ion storage.[56,57] The CV and GCD curves also showed electric double-layer capacitance features at a scan rate in the range of 5–200 mV s^{-1} (Fig. S4a†) and a typical triangular shape under different current densities in the range of 0.2–50 A g^{-1} (Fig. S4b†). Fig. 4c presents the rate capability for both GQDs/Gr- and AL-based electrodes at a current density in the range from 0.1 to 50 A g^{-1}. The specific capacitance decreased from 404.6 F g^{-1} to 210 F g^{-1} with 53% retention compared to that of AL with 162 F g^{-1} decreasing to 60 F g^{-1} with only 37% retention when the current density was raised from 0.1 A g^{-1} to 50 A g^{-1}. The highly dispersed and crystalline GQDs/Gr with high conductivity and good porosity endow it relatively high retention of capacitance for efficient ion storage and diffusion,[28,42] and the attenuation caused by the GQDs sites.

The ion-transport behavior and electrical resistance were investigated by electrochemical impedance spectroscopy (EIS). Fig. 4d gives the Nyquist plots for both the GQDs/Gr- and AL-based electrode in the frequency range from 10^{-2} to 10^{5} Hz, and both the plots sharply rose up and tended to a vertical line, indicative of ideal capacitive behavior. The phase angle of −87° for GQDs/Gr was higher than that for AL of −80°, which evidences its better capacitive behavior. The enlarged high-frequency region was with the impedances of (inset of Fig. 4d) the axis intercept and the diameter of the semi-circle represent the equivalent series resistance (ESR) and interfacial charge-transfer resistance, respectively. The GQD/Gr electrode presents a relatively high ESR of 0.684 Ω compared with that of the AL electrode of 0.61 Ω, and significantly lower charge-transfer resistance with 3.6 times resistance of 0.344 Ω than that of AL of 1.24 Ω, the GQDs/Gr electrode has a 7 times greater knee frequency of 317 Hz than that of AL of 46.4 Hz, which proved much faster charge/ion transport between the electrodes and the electrolyte. The phase angle of GQDs/Gr is close to −90° at low frequency, which exhibits a capacitive behavior.[26,58] It reaches −45° for GQDs/Gr with a characteristic frequency (f_0) of 3.3 Hz corresponding to a time constant (τ_0) of 0.3 s, which was 7.5 times faster than that of AL with 0.43 Hz and 2.3 s, which is also much faster than that of previous reports for τ_0 (Tables S1, S2, and Fig. S5†).[25,59–61] The capacitance, stability, and τ_0 were fully compared with other biomass-based and GQD strategy modified supercapacitors with better performance for GQDs/Gr, as shown in Tables S1 and S2,† respectively. The quite lower charge-transfer resistance and f_0 of GQDs/Gr than AL could be attributed to the well-ordered lattice for both the GQDs and the graphene sheet having a higher conductivity,[9] which boosted

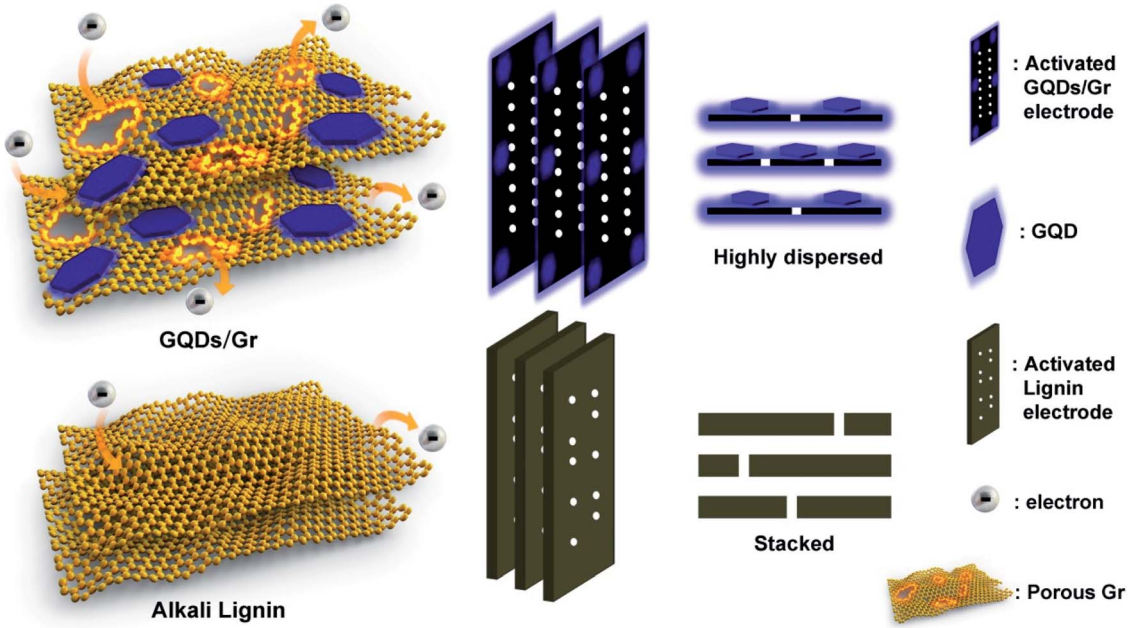

Fig. 5 Schematic illustration of GQD/Gr and alkali lignin electrode, indicative of more electron storage and efficient diffusion towards the GQD/Gr electrode.

the efficient electron transport. Furthermore, the highly dispersed graphene sheets with the addition of GQDs more easily exposed numerous pores, which was helpful in contacting with the electrolyte and undertake more electrons. The abundant connected pore structure more easily allowed electrolyte ion penetration and diffusion, which was consistent with the fast charge transporting behavior.[42,59–64] Fig. 4f reflected the cycle stability at a high current density of 10 A g^{-1}, which still maintained 97% retention even after 10 000 charge/discharge cycles in spite of the slight decrease after 8000 cycles. We infer that the good cycle stability could be attributed to the highly crystalline structure of the GQD/Gr hetero-junction and stable interaction between the GQD and the Gr sheet.

We further rationalized the mechanism of simultaneous fast charging and boosted specific capacitance with 7.5 times faster charging speed and 2.5 times higher capacitance than that of the AL-based electrode. Fig. 5 gives a general description of the GQD/Gr- and AL-based electrodes. The AL electrode could easily stack into activated carbon with a jammed pore structure, while the porous graphene sheet and the attached GQDs-assembled highly dispersed GQD/Gr hetero-junction could enable highly efficient ionic diffusion and increased number of active sites for ion storage.[3] The transition from lignin to GQDs and then refusion into graphene provided the *in situ* growth of GQDs on the graphene, which resulted in good interfacial compatibility with the GQD/Gr hetero-junction, endowing more conductive linkages with lower electric resistances. In addition, the GQDs function as nano-additives between the Gr layers for effective restraint from the stack, thus efficiently enlarging the distance between the graphene layers with massive electron capacitive sites and more hierarchical channels (Fig. 5).

4 Conclusion

In this work, the all-lignin based novel GQD/Gr hetero-junction was designed to simultaneously promote the storage sites and diffusion kinetics with boosted specific capacitance and ultrafast charging–discharging speed. The conversion mechanism of GQDs/Gr was systematically studied, consisting of lignin aromatic rebonding, aromatic refusion into GQDs, and aromatic enlargement into the GQDs/Gr. The GQDs play an additive role for preventing the stacks and agglomerates between the graphene layers, which endow the assembled GQD/Gr hetero-junction with massive electron capacitive sites and more hierarchical channels. Therefore, this designed junction could simultaneously achieve high specific capacitance and ultrafast charging–discharging speed with a boosted specific capacitance of 404.6 F g^{-1} and a short reaction time constant (τ_0) of 0.3 s, which were 2.5 times higher and 7.5 times faster than that of unmodified lignin electrode with 162 F g^{-1} and 2.3 s, respectively. A power density of 225 W kg^{-1} and energy density of 35.1 W h kg^{-1} were calculated. More importantly, this proposed strategy could offer the opportunity to unblock the critical roadblocks for all-lignin based superior supercapacitors by composing a 0D/2D π-conjugated GQDs/Gr hetero-junction system and also open a new window for the high value industrial lignin conversion into cheap, sustainable, and high-performance electrochemical energy devices.

Author contributions

Z. Y. Ding and X. L. Wang conceived the idea and prepared the manuscript. X. L. Wang supervised the project. Z. Y. Ding conducted major characterization analysis and data curation. X. W.

Mei carried out all the electrochemical test and BET analysis. All authors analyzed the data, discussed the results and assisted with manuscript preparation.

Conflicts of interest

There are no conflicts to declare.

Acknowledgements

This work was supported by the National Natural Science Foundation of China (51603012).

Notes and references

1 S. Liu, J. Xu, J. Zhu, Y. Chang, H. Wang, Z. Liu, Y. Xu, C. Zhang and T. Liu, *J. Mater. Chem. A*, 2017, **5**, 19997–20004.
2 J. Zhao, J. Zhu, Y. Li, L. Wang, Y. Dong, Z. Jiang, C. Fan, Y. Cao, R. Sheng and A. Liu, *ACS Appl. Mater. Interfaces*, 2020, **12**, 11669–11678.
3 J. Zhu, J. Roscow, S. Chandrasekaran, L. Deng, P. Zhang, T. He, K. Wang and L. Huang, *ChemSusChem*, 2020, **13**, 1275–1295.
4 X. Wu, J. Jiang, C. Wang, J. Liu, Y. Pu, A. Ragauskas, S. Li and B. Yang, *Biofuels, Bioprod. Biorefin.*, 2020, **14**, 650–672.
5 C. Heitner, D. Dimmel and J. Schmidt, *Lignin and lignans: advances in chemistry*, CRC press, 2016.
6 Z. Fang and R. L. Smith Jr, *Production of biofuels and chemicals from lignin*, Springer, 2016.
7 X. Zhao, H. Chen, F. Kong, Y. Zhang, S. Wang, S. Liu, L. A. Lucia, P. Fatehi and H. Pang, *Chem. Eng. J.*, 2019, **364**, 226–243.
8 J. Becker and C. Wittmann, *Biotechnol. Adv.*, 2019, **37**, 107360.
9 Z. Ding, T. Yuan, J. Wen, X. Cao, S. Sun, L. Xiao, Q. Shi, X. Wang and R. Sun, *Carbon*, 2020, **158**, 690–697.
10 Z. Ding, F. Li, J. Wen, X. Wang and R. Sun, *Green Chem.*, 2018, **20**, 1383–1390.
11 R. Ye, Y. Chyan, J. Zhang, Y. Li, X. Han, C. Kittrell and J. M. Tour, *Adv. Mater.*, 2017, **29**, 1702211.
12 C. Shi, L. Hu, K. Guo, H. Li and T. Zhai, *Adv. Sustainable Syst.*, 2017, **1**, 1600011.
13 W. Zhang, Y. Lei, F. Ming, Q. Jiang, P. M. Costa and H. N. Alshareef, *Adv. Energy Mater.*, 2018, **8**, 1801840.
14 J. W. Jeon, L. Zhang, J. L. Lutkenhaus, D. D. Laskar, J. P. Lemmon, D. Choi, M. I. Nandasiri, A. Hashmi, J. Xu and R. K. Motkuri, *ChemSusChem*, 2015, **8**, 428–432.
15 C. D. Tran, H. C. Ho, J. K. Keum, J. Chen, N. C. Gallego and A. K. Naskar, *Energy Technol.*, 2017, **5**, 1927–1935.
16 P. Schlee, O. Hosseinaei, C. A. O' Keefe, M. J. Mostazo-López, D. Cazorla-Amorós, S. Herou, P. Tomani, C. P. Grey and M.-M. Titirici, *J. Mater. Chem. A*, 2020, **8**, 23543–23554.
17 C. Xiong, M. Li, W. Zhao, C. Duan, L. Dai, M. Shen, Y. Xu and Y. Ni, *Chem. Eng. J.*, 2020, **396**, 125318.
18 C. Xiong, B. Li, H. Liu, W. Zhao, C. Duan, H. Wu and Y. Ni, *J. Mater. Chem. A*, 2020, **8**, 10898–10908.
19 C. Xiong, X. Lin, H. Liu, M. Li, B. Li, S. Jiao, W. Zhao, C. Duan, L. Dai and Y. Ni, *J. Electrochem. Soc.*, 2019, **166**, A3965–A3971.
20 C. Xiong, M. Li, W. Zhao, C. Duan and Y. Ni, *J. Materiomics*, 2020, **6**(3), 523–531.
21 C. Xiong, M. Li, S. Nie, W. Dang, W. Zhao, L. Dai and Y. Ni, *J. Power Sources*, 2020, **471**, 228448.
22 X. Zhang, X. Cui, C.-H. Lu, H. Li, Q. Zhang, C. He and Y. Yang, *Chem. Eng. J.*, 2020, **401**, 126031.
23 X. Zhang, H. Li, W. Zhang, Z. Huang, C. P. Tsui, C. Lu, C. He and Y. Yang, *Electrochim. Acta*, 2019, **301**, 55–62.
24 X. Zhang, J. Zhao, X. He, Q. Li, C. Ao, T. Xia, W. Zhang, C. Lu and Y. Deng, *Carbon*, 2018, **127**, 236–244.
25 Z. Peng, Y. Zou, S. Xu, W. Zhong and W. Yang, *ACS Appl. Mater. Interfaces*, 2018, **10**, 22190–22200.
26 F. Li, X. Wang and R. Sun, *J. Mater. Chem. A*, 2017, **5**, 20643–20650.
27 W. Tian, J. Zhu, Y. Dong, J. Zhao, J. Li, N. Guo, H. Lin, S. Zhang and D. Jia, *Carbon*, 2020, **161**, 89–96.
28 B. Chang, Y. Guo, Y. Li, H. Yin, S. Zhang, B. Yang and X. Dong, *J. Mater. Chem. A*, 2015, **3**, 9565–9577.
29 F. Fu, D. Yang, W. Zhang, H. Wang and X. Qiu, *Chem. Eng. J.*, 2019, **392**, 123721.
30 X. Zhao, M. Li, H. Dong, Y. Liu, H. Hu, Y. Cai, Y. Liang, Y. Xiao and M. Zheng, *ChemSusChem*, 2017, **10**, 2626–2634.
31 B. Chang, H. Yin, X. Zhang, S. Zhang and B. Yang, *Chem. Eng. J.*, 2017, **312**, 191–203.
32 S. Sankar, H. Lee, H. Jung, A. Kim, A. T. A. Ahmed, A. I. Inamdar, H. Kim, S. Lee, H. Im and D. Y. Kim, *New J. Chem.*, 2017, **41**, 13792–13797.
33 F. J. García-Mateos, R. Berenguer, M. J. Valero-Romero, J. Rodríguez-Mirasol and T. Cordero, *J. Mater. Chem. A*, 2018, **6**, 1219–1233.
34 T. Zhao, X. Ji, P. Bi, W. Jin, C. Xiong, A. Dang, H. Li, T. Li, S. Shang and Z. Zhou, *Electrochim. Acta*, 2017, **230**, 342–349.
35 Y. Li, Z. Li and P. K. Shen, *Adv. Mater.*, 2013, **25**, 2474–2480.
36 Q. Cheng, J. Tang, N. Shinya and L.-C. Qin, *J. Power Sources*, 2013, **241**, 423–428.
37 R. R. Salunkhe, S. H. Hsu, K. C. Wu and Y. Yamauchi, *ChemSusChem*, 2014, **7**, 1551–1556.
38 F. N. Ajjan, N. Casado, T. Rębiś, A. Elfwing, N. Solin, D. Mecerreyes and O. Inganäs, *J. Mater. Chem. A*, 2016, **4**, 1838–1847.
39 W. Tan, R. Fu, H. Ji, Y. Kong, Y. Xu and Y. Qin, *Int. J. Biol. Macromol.*, 2018, **112**, 561–566.
40 Z. Li, Y. Li, L. Wang, L. Cao, X. Liu, Z. Chen, D. Pan and M. Wu, *Electrochim. Acta*, 2017, **235**, 561–569.
41 H. Wang, B. Wang, D. Sun, Q. Shi, L. Zheng, S. Wang, S. Liu, R. Xia and R. Sun, *ChemSusChem*, 2019, **12**, 1059–1068.
42 C. Cui, Y. Gao, J. Li, C. Yang, M. Liu, H. Jin, Z. Xia, L. Dai, Y. Lei and J. Wang, *Angew. Chem. Int. Ed.*, 2020, **59**, 7928.
43 S. H. Jin, D. H. Kim, G. H. Jun, S. H. Hong and S. Jeon, *ACS Nano*, 2013, **7**, 1239–1245.
44 L. Wang, Y. Wang, T. Xu, H. Liao, C. Yao, Y. Liu, Z. Li, Z. Chen, D. Pan and L. Sun, *Nat. Commun.*, 2014, **5**, 5357.
45 Y. Yan, D. Zhai, Y. Liu, J. Gong, J. Chen, P. Zan, Z. Zeng, S. Li, W. Huang and P. Chen, *ACS Nano*, 2020, **14**(1), 1185–1195.

46 Q. Li, M. T. Naik, H.-S. Lin, C. Hu, W. K. Serem, L. Liu, P. Karki, F. Zhou and J. S. Yuan, *Carbon*, 2018, **139**, 500–511.
47 W.-J. Liu, H. Jiang and H.-Q. Yu, *Green Chem.*, 2015, **17**, 4888–4907.
48 P. Schlee, O. Hosseinaei, D. Baker, A. Landmér, P. Tomani, M. J. Mostazo-López, D. Cazorla-Amorós, S. Herou and M.-M. Titirici, *Carbon*, 2019, **145**, 470–480.
49 B. M. Upton and A. M. Kasko, *Chem. Rev.*, 2015, **116**, 2275–2306.
50 Y. Le Brech, L. Delmotte, J. Raya, N. Brosse, R. Gadiou and A. Dufour, *Anal. Chem.*, 2015, **87**, 843–847.
51 R. S. Jordan, Y. L. Li, C. W. Lin, R. D. Mccurdy and Y. Rubin, *J. Am. Chem. Soc.*, 2017, **139**, 15878–15890.
52 X. Li, W. Cai, J. An, S. Kim, J. Nah, D. Yang, R. Piner, A. Velamakanni, I. Jung and E. Tutuc, *Science*, 2009, **324**, 1312.
53 G. Zhao, X. Li, M. Huang, Z. Zhen, Y. Zhong, Q. Chen, X. Zhao, Y. He, R. Hu and T. Yang, *Chem. Soc. Rev.*, 2017, **46**, 4417–4449.
54 J. Zhu, Y. Huang, W. Mei, C. Zhao, C. Zhang, J. Zhang, I. S. Amiinu and S. Mu, *Angew. Chem., Int. Ed.*, 2019, **58**, 3859–3864.
55 L. Liu, H. Zhao and Y. Lei, *InfoMat*, 2019, **1**, 74–84.
56 F. Liu, L. Xie, L. Wang, W. Chen, W. Wei, X. Chen, S. Luo, L. Dong, Q. Dai and Y. Huang, *Nano-Micro Lett.*, 2020, **12**, 17.
57 Z. Bi, Q. Kong, Y. Cao, G. Sun, F. Su, X. Wei, X. Li, A. Ahmad, L. Xie and C.-M. Chen, *J. Mater. Chem. A*, 2019, **7**, 16028–16045.
58 Q. Shao, J. Tang, Y. Lin, J. Li, F. Qin, J. Yuan and L.-C. Qin, *J. Power Sources*, 2015, **278**, 751–759.
59 Y. Li, G. Wang, T. Wei, Z. Fan and P. Yan, *Nano Energy*, 2016, **19**, 165–175.
60 D. Saha, Y. Li, Z. Bi, J. Chen, J. K. Keum, D. K. Hensley, H. A. Grappe, H. M. Meyer III, S. Dai and M. P. Paranthaman, *Langmuir*, 2014, **30**, 900–910.
61 S. Leguizamon, K. P. Díaz-Orellana, J. Velez, M. C. Thies and M. E. Roberts, *J. Mater. Chem. A*, 2015, **3**, 11330–11339.
62 F. Zhou, H. Huang, C. Xiao, S. Zheng, X. Shi, J. Qin, Q. Fu, X. Bao, X. Feng and K. Müllen, *J. Am. Chem. Soc.*, 2018, **140**, 8198–8205.
63 Z. Dai, P.-G. Ren, Y.-L. Jin, H. Zhang, F. Ren and Q. Zhang, *J. Power Sources*, 2019, **437**, 226937.
64 T. Kim, G. Jung, S. Yoo, K. S. Suh and R. S. Ruoff, *ACS Nano*, 2013, **7**, 6899–6905.